

Ubiquitous formation of type-II bulk Dirac cones and topological surface states from a single orbital manifold in transition-metal dichalcogenides

M. S. Bahramy^{1,2,*†}, O. J. Clark^{3,*}, B.-J. Yang^{4,5,6}, J. Feng³, L. Bawden³, J. M. Riley^{3,7}, I. Marković^{3,8}, F. Mazzola³, V. Sunko^{3,8}, D. Biswas³, S. P. Cooil⁹, M. Jorge⁹, J. W. Wells⁹, M. Leandersson¹⁰, T. Balasubramanian¹⁰, J. Fujii¹¹, I. Vobornik¹¹, J. Rault¹², T. K. Kim⁷, M. Hoesch⁷, K. Okawa¹³, M. Asakawa¹³, T. Sasagawa¹³, T. Eknapakul¹⁴, W. Meevasana^{14,15}, P. D. C. King^{3,‡}

¹ Quantum-Phase Electronics Center and Department of Applied Physics,

The University of Tokyo, Tokyo 113-8656, Japan

² RIKEN center for Emergent Matter Science (CEMS), Wako 351-0198, Japan

³ SUPA, School of Physics and Astronomy, University of St. Andrews, St. Andrews, Fife KY16 9SS, United Kingdom

⁴ Department of Physics and Astronomy, Seoul National University, Seoul 08826, Korea

⁵ Center for Correlated Electron Systems, Institute for Basic Science (IBS), Seoul 08826, Korea

⁶ Center for Theoretical Physics (CTP), Seoul National University, Seoul 08826, Korea

⁷ Diamond Light Source, Harwell Campus, Didcot, OX11 0DE, United Kingdom

⁸ Max Planck Institute for Chemical Physics of Solids, Nöthnitzer Straße 40, 01187 Dresden, Germany

⁹ Department of Physics, Norwegian University of Science and Technology (NTNU), N-7491 Trondheim, Norway

¹⁰ MAX IV Laboratory, Lund University, P. O. Box 118, 221 00 Lund, Sweden

¹¹ Istituto Officina dei Materiali (IOM)-CNR, Laboratorio TASC, in Area Science Park, S.S.14, Km 163.5, IW34149 Trieste, Italy

¹² Synchrotron SOLEIL, CNRS-CEA, L'Orme des Merisiers, Saint-Aubin-BP48, 91192 Gif-sur-Yvette, France

¹³ Laboratory for Materials and Structures, Tokyo Institute of Technology, Kanagawa 226-8503, Japan

¹⁴ School of Physics, Suranaree University of Technology, Nakhon Ratchasima, 30000, Thailand

¹⁵ NANOTEC-SUT Center of Excellence on Advanced Functional Nanomaterials, Suranaree University of Technology, Nakhon Ratchasima 30000, Thailand

* These authors contributed equally to this work

† To whom correspondence should be addressed: bahramy@ap.t.u-tokyo.ac.jp and

‡ To whom correspondence should be addressed: philip.king@st-andrews.ac.uk

(Dated: February 28, 2017)

Transition-metal dichalcogenides (TMDs) are renowned for their rich and varied properties. They range from metals and superconductors^{1–3} to strongly spin-orbit-coupled semiconductors^{4,5} and charge-density-wave systems,^{6–8} with their single-layer variants one of the most prominent current examples of two-dimensional materials beyond graphene.^{4,9} Their varied ground states largely depend on the transition metal d -electron-derived electronic states, on which the vast majority of attention has been concentrated to date.^{4,7,10–16} Here, we focus on the chalcogen-derived states. From density-functional theory calculations together with spin- and angle-resolved photoemission, we find that these generically host type-II three-dimensional bulk Dirac fermions as well as ladders of topological surface states and surface resonances. We demonstrate how these naturally arise within a single p -orbital manifold as a general consequence of a trigonal crystal field, and as such can be expected across a large number of compounds. Already, we demonstrate their existence in six separate TMDs, opening routes to tune, and ultimately exploit, their topological physics.

The classification of electronic structures based on

their topological properties has opened new paradigms for understanding solid state materials.¹⁷ The now-familiar \mathbb{Z}_2 topological insulators are most renowned for their spin-polarised Dirac surface states residing in inverted bulk band gaps.¹⁷ In systems with rotational invariance, a band inversion on the rotation axis can generate protected Dirac cones with a point-like Fermi surface of the bulk electronic structure.^{18–24} Such states are similar to a three-dimensional version of the well-known Dirac dispersions in graphene, but additionally host exotic arc-like surface states that span the surface projections of the bulk Dirac points.^{25,26} If the strict requirement of spin degeneracy of the bulk electronic structure is lifted by breaking either inversion or time-reversal symmetry, a bulk Dirac point can split into a pair of Weyl points, which host their own surface Fermi arcs.^{27–33} Unlike for elementary particles, Lorentz-violating Weyl fermions can also exist in the solid state, manifested as strongly tilted (so-called type-II) Weyl cones which occur at the touching of bulk electron and hole pockets.³⁴

Realising such phases in solid-state materials not only offers new environments and opportunities for studying the fundamental properties of fermions, but also holds the potential for advancing new technological applications, for example within spin-based electronics. Consequently, there is an intense current effort focused on

identifying compounds which host the requisite band inversions to stabilise this ever-increasing array of different topologically non-trivial states and phases. In many cases, however, this depends sensitively on fine details of a material's electronic or crystal structure. For example, the spin-orbit mediated band inversion which stabilises the prototypical \mathbb{Z}_2 topological insulator phase in Bi_2Se_3 occurs due to an inversion of Bi and Se p_z orbitals, while a reduction in spin-orbit coupling strength on moving to Sb_2Se_3 renders this compound topologically trivial.³⁵ Meanwhile, the number, type (I or II), and even existence of Weyl points in the electronic structure of the recently predicted type-II Weyl semimetals WTe_2 and MoTe_2 has been argued to be extremely sensitive to small lattice strains.^{34,36} Such sensitivity dramatically complicates the search for new topologically non-trivial materials.

Almost all known topologically non-trivial phases are stabilised by band inversions between states derived predominantly from different atomic manifolds (e.g. Bi and Se p orbitals in Bi_2Se_3 ,³⁵ Bi p and Na s orbitals in Na_3Bi ,²⁰ Nb d and P p orbitals in NbP ³⁷), partly explaining such sensitivity to varying material parameters. In contrast, here we uncover a simple and remarkably robust mechanism for realising a hierarchy of band inversions within a single orbital manifold. We demonstrate, both theoretically and experimentally, how a k_z -dependent band inversion of p -orbitals alone is sufficient to drive the formation of strongly-tilted type-II bulk Dirac cones as well as ladders of topological surface states (TSSs) and topological surface resonances in the transition-metal dichalcogenide (TMD) superconductor PdTe_2 . We also observe and classify how similar band inversions generate bulk Dirac points (BDPs) and TSSs across the family of 2H- and 1T-structured TMDs. The resilience of these states to changing crystal structure, varying degrees of d - p orbital mixing, and disparate bulk properties of the compounds we investigate points to the generic nature of our findings, and to the key importance of topological phenomena across the TMD material class.

Figure 1 details the general principle underlying our findings. As a minimal model, we consider a 2-site model with space group C_{3v} , with 3×2 p -orbitals per site in a trigonal crystal field. Such an arrangement naturally describes, for example, the chalcogen layers of the 1T-TMDs (Fig. 1(a)), although we neglect the presence of the transition-metal atom located between the chalcogen planes in that structure in our initial discussions. Bonding and anti-bonding (BA) combinations of the p -orbital derived states form triply-degenerate (neglecting spin) manifolds, which are each split by the trigonal crystal field into a doubly-degenerate E level (formed from p_x and p_y orbitals) above (bonding) or below (anti-bonding) a single A_1 (p_z -derived) level (Fig. 1(c)). Including spin-orbit coupling (SOC), the A_1 level transforms into the double representation R_4^\pm ($|J| = 1/2; |m_J| = 1/2$) and

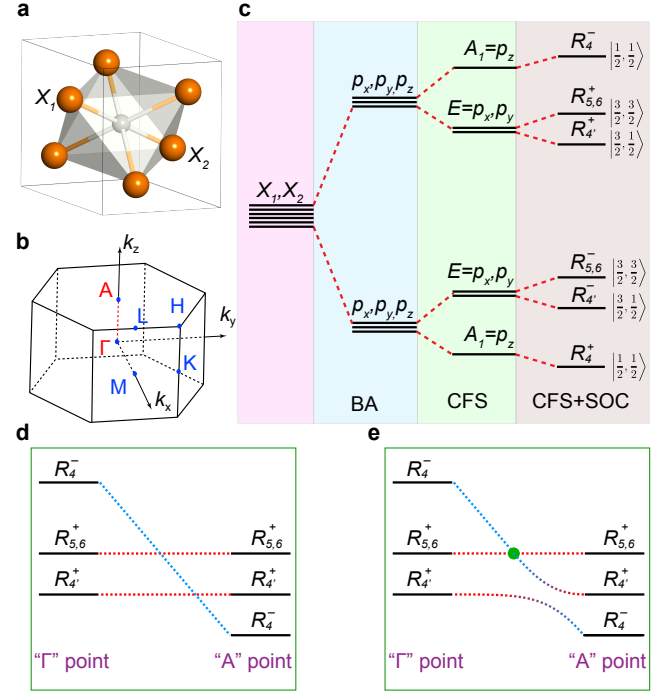


FIG. 1. Hierarchy of band inversions arising from p orbitals in a trigonal crystal field. (a) Crystal structure of the 1T transition-metal dichalcogenides, with the transition metal at the centre of a trigonally-distorted octahedron of chalcogen atoms (X_1 and X_2) which each form triangular layers above and below the transition-metal plane. The corresponding Brillouin zone is shown in (b). (c) Schematic illustration of the orbital energy level evolution of p -orbitals on the chalcogen site when considering bonding/anti-bonding (BA), a trigonal crystal field splitting (CFS) and spin-orbit coupling (SOC). (d,e) Evolution of these crystal field-derived levels (anti-bonding set) as a function of out-of-plane momentum, showing a crossing of the A_1 and E -derived levels that is naturally expected due to their disparate out-of-plane dispersion. Hybridisation is neglected in (d) but included in (e), showing the resulting formation of a protected crossing and the opening of an inverted band gap with \mathbb{Z}_2 topological order at the crossing of the R_4^- level with the $R_{5,6}^+$ and R_4^+ levels, respectively. The superscript \pm indicates the parity of each level.

the E manifold further splits into an upper $R_{5,6}^\mp$ ($|J| = 3/2; |m_J| = 3/2$) and a lower $R_{4'}^\mp$ ($|J| = 3/2; |m_J| = 1/2$) level. Here, the superscript \pm indicates the parity of each level which, as shown in Fig. 1(c) for a given representation, can be either $+$ (even parity) or $-$ (odd parity) depending on its bonding nature.

We now consider band formation, and in particular the evolution of the electronic states derived from these orbital energy levels as a function of the out-of-plane momentum. The out-of-plane p_z orbitals will have much larger hopping along the out-of-plane direction than the in-plane orbitals. For simplicity, we therefore initially completely neglect inter-layer hopping of the in-plane

p orbitals in this simple example. This leads to dispersionless E -derived levels as a function of the out-of-plane momentum, k_z , while the A_1 bands retain a strong k_z -dispersion (Fig. 1(d)). When the bandwidth arising due to inter-layer hopping becomes larger than the crystal field splitting (CFS), the A_1 -derived band will cross through the E -derived ones, creating a set of k_z -dependent band inversions solely within the p -orbital derived manifold of states. In general, one would expect the bands to hybridise and open up anti-crossing gaps at these intersections. This is indeed what should occur at the crossings of R_4^\pm with $R_{4'}^\mp$ bands (Fig. 1(e)), as they both share the same symmetry character and the same angular momentum $m_J = 1/2$. They have opposite parity, however, and thus their hybridization leads to an inverted band gap with a \mathbb{Z}_2 topological order. Accordingly, these gaps can be expected to host topological surface states, as we demonstrate below.

The R_4^\pm and $R_{5,6}^\mp$ -derived bands, on the other hand, belong to different irreducible representations. As a result, they behave differently under the application of the rotational operator C_{3v} : for example, the rotational eigenvalue of $R_{4'}^\pm$ with $m_J = 1/2$ is $e^{\frac{2\pi i}{3}m_J} = e^{\frac{\pi i}{3}}$ whereas it is equal to -1 for $R_{5,6}^\mp$ with $m_J = 3/2$. Hence, for a given Hamiltonian $H(k)$, the hybridization matrix element $\langle R_4 | H(k) | R_{5,6} \rangle$ is zero and the crossing of these bands is protected against hybridization as long as it occurs at a k -point with C_{3v} symmetry and the host system has both inversion and time-reversal symmetries.^{18,23,24} For the model considered here, this is satisfied for all k -points along the Γ -A direction of the three-dimensional Brillouin zone ($k_x = k_y = 0$, varying k_z , see Fig. 1(b)). Consequently, the crossing of the R_4^\pm and $R_{5,6}^\mp$ -derived bands will lead to a single point of degeneracy (i.e., a bulk Dirac point) located part-way along this direction. Its location in momentum space is set both by the bandwidth of the R_4^\pm -derived band and by the strength of the CFS. In the schematic shown here (Fig. 1(e)), one branch of the Dirac cone is highly dispersive along k_z while the other is completely dispersionless. While, in reality, the $R_{5,6}^\mp$ -derived band can still have a finite out-of-plane dispersion due to non-zero inter-layer coupling even for the in-plane atomic orbitals from which it derives, its group velocity will typically be much smaller than that of the R_4^\mp -derived band. The resulting Dirac cone will remain strongly tilted: the Dirac fermions will therefore be of the so-called type-II (Lorentz-violating) classification, in analogy to the recent classification of type-II Weyl fermions.³⁴

We show in Fig. 2 that this simple model can be realised surprisingly well in the near-Fermi level electronic structure of the TMD superconductor³⁹ 1T-PdTe₂. Its crystal structure (space group: $P\bar{3}m1$) is composed of edge-sharing PdTe₆ octahedra, although a strong suppression of c/a as compared to that of “ideal” octahedral co-ordination (where c and a are the out-of-plane and

in-plane lattice constants, respectively) points to a significant trigonal distortion.³⁸ Pd acts as a cation with a nominal valence state 2+. However, these valence electrons do not contribute effectively to the Pd-Te bonds. Rather they preferentially form strong metallic bonds between the neighbouring Pd atoms and do not contribute significantly to conductivity in this system. This is supported by our first-principles calculations of the orbitally-resolved electronic structure (Fig. 2(a)), which show that the majority of the weight of the transition-metal d -orbitals are between ~ 1.8 and 6.5 eV below the Fermi level. The deficiency in charge transfer from Pd to Te leaves the p orbitals of Te partially unoccupied. This can be partly compensated by a covalent bonding between adjacent Te ions through an intra-layer hopping between the $p_{x,y}$ orbitals as well as an inter-layer hopping between the p_z orbitals. Importantly, this can be expected to lead to a strong k_z dispersion for those energy bands dominated by Te- p_z orbitals.

These features can be readily identified in our electronic structure calculations. Focussing along the Γ -A direction (Fig. 2(a)), two pairs of predominantly Te $p_{x,y}$ -derived bands can be seen within the energy region $E - E_F \sim -1$ to ~ 2 eV (red colouring in Fig. 2(a)), which we assign as the bonding and anti-bonding E bands in analogy with the discussion above. Each are split by the combined influence of CFS and SOC, and each has only modest out-of-plane dispersion, although much more significant dispersion can be observed along the in-plane directions consistent with their in-plane orbital character. In contrast, the p_z - (A_1)-derived states (cyan colouring in Fig. 2(a)) have a dispersion along Γ -A that spans nearly the entire valence band bandwidth, and thus crosses through the E states as a function of k_z . Above the Fermi level, where the R_4^- band intersects the anti-bonding $R_{5,6}^+$ and $R_{4'}^+$ states, a clear protected and avoided crossing are formed, respectively, entirely consistent with the simple picture outlined above. A similar phenomenology is observed for the bands immediately below E_F : the first crossing of the p_z -derived band with the bonding $R_{5,6}^-$ states leads to another protected BDP, while the second crossing is again gapped. In fact, the proximity of this final crossing to both the anti-bonding and bonding-like branches of the p_z -derived bands causes an additional inverted gap to open directly below this. The deeper one is generated directly by the anti-crossing of bonding R_4^+ and $R_{4'}^-$ states, evident from a small kink structure near the A-point of the R_4' band. The shallower band gap results from the crossing of bonding R_4' with both anti-bonding R_4 and bonding R_4 states. As the latter two states have opposite parities the total parity of the lower band at the A-point becomes opposite to that at the Γ -point, and hence this is also an inverted band gap with \mathbb{Z}_2 topological order.

These features are well reproduced by our photon energy-dependent angle-resolved-photoemission

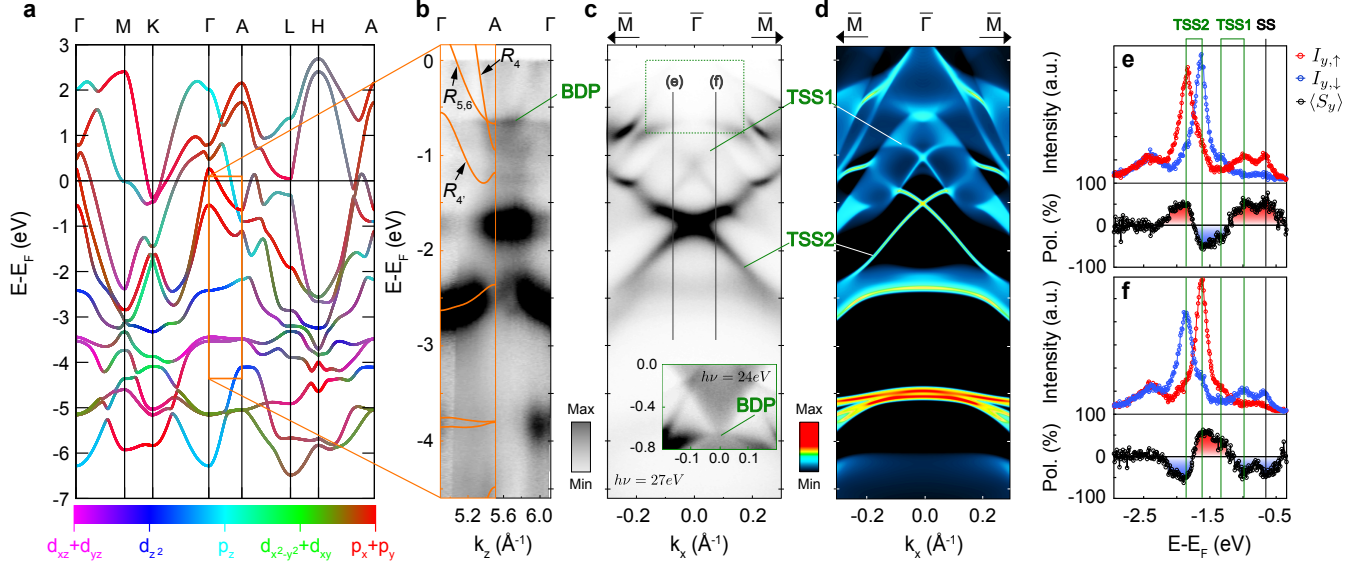


FIG. 2. **Chalcogen-derived topological ladder in PdTe₂.** (a) Orbitally-resolved bulk electronic structure of PdTe₂, indicating dominantly chalcogen-derived orbital character for the states in the vicinity of the Fermi level. (b) Our ARPES measurements ($h\nu = 80 - 132$ eV, $k_x = k_y = 0$) well reproduce the calculated out-of-plane dispersion when the calculations are rescaled by a factor of 1.08 (solid lines), revealing the formation of bulk Dirac points (BDPs) and gapped crossings of the upper p_z and $p_{x,y}$ -derived states. The corresponding bulk Dirac cones and topological surface states located within the inverted band gaps are clearly observed (c) in our ARPES measurements ($h\nu = 27$ eV (24 eV for inset)) and (d) supercell calculations (projected onto the first 2 unit cells, see methods) along the $\bar{\Gamma}-\bar{M}$ direction. (e,f) Spin-resolved energy distribution curves along the lines shown in (c) reveal a clear helical spin texture of the two topological surface states (TSS1 & 2), with an up-down-down-up relative ordering, as well as an additional spin-polarised state above TSS1 which we label SS.

(ARPES) measurements of the occupied electronic structure (Fig. 2(b)). While the measured spectral features are broadened due to the finite k_z -resolution of photoemission, a significant k_z dispersion of a number of states along Γ -A can still be observed. In the vicinity of E_F , we observe a light and more massive band which cross at a binding energy of ~ 0.6 eV at a k_z position close to a bulk A-point. This is entirely consistent with our calculations, and with the presence of a type-II bulk Dirac cone near to the Brillouin zone boundary along the Γ -A line (see also Supplemental Fig. S1). To further confirm this, we measure the in-plane dispersion of these same states along $\bar{\Gamma}-\bar{M}$ (inset of Fig. 2(c)) and $\bar{\Gamma}-\bar{K}$ (inset of Fig. 3(c)) of the surface Brillouin zone, where we observe diffuse “filled-in” intensity forming the upper part of a Dirac cone-like feature. These measurements integrate over a significant portion of the Brillouin zone along k_z for the low photon energy used, and thus the diffuse nature of these states points to their three-dimensionality. Nonetheless, the apex of our observed cone, located ~ 0.6 eV below E_F , is in agreement with the crossing point of the bulk bands observed in our photon energy-dependent measurements along Γ -A, as well as with our theoretical calculations. Together, these observations and calculations therefore identify the presence of type-II Dirac cones in PdTe₂,

arising due to the protected crossing of Te p_z - and $p_{x,y}$ -crystal field-split states as they disperse differently with out-of-plane momentum.⁴¹ We note that spectroscopic signatures of the bulk Dirac cone (inset to Fig. 2(c)) extend up to the Fermi level and hence these Dirac fermions may carry signatures in transport measurements.⁴⁰

Additional states which are non-dispersive in k_z , and are thus two-dimensional, are also evident in our photon energy-dependent measurements. Most prominent is a band visible in Fig. 2(b) at $E - E_F \sim 1.7$ eV, an energy at which no bulk states are present along Γ -A. We thus assign this as a surface state. Its in-plane dispersion (Fig. 2(c)) shows a clear Dirac-like dispersion in the vicinity of $\bar{\Gamma}$, and is well reproduced by our supercell calculations of the surface electronic structure (Fig. 2(d) and Supplemental Fig. S2, see Methods) confirming its surface-derived origin. This has recently been observed by Yan *et al.*⁴² and assigned as a topological surface state. Our measurements and calculations fully support this assignment: we find that it is located within the k_z -projected band gap that arises from the lower of the two avoided crossings below the Fermi level, between the R_4^+ and R_4^- bands identified above. To definitively identify its topological nature, we perform additional spin-resolved ARPES measurements (Fig. 2(e) and Supple-

mental Fig. S3). These reveal that this state is indeed strongly spin-polarised (from fits to EDCs, we find an in-plane spin polarisation of $92 \pm 14\%$ ($73 \pm 16\%$) for the upper (lower) branch of this surface state) with the spin lying almost entirely within the surface plane, locked perpendicular to the in-plane momentum. Moreover, the sign of the spin polarisation reverses on opposite sides of, as well as above and below, the Dirac point where the two branches of the surface state cross at $\bar{\Gamma}$. This is a hallmark signature of the spin-helical surface states of topological insulators: we refer below to this topological surface state as TSS2.

More subtly, our supercell calculations also reveal an additional surface-localised state forming another two-dimensional Dirac cone-like feature located at the energy of the band gap opened by the crossing of the R_4^- and R_{4f} bands. Unlike for TSS2, however, the band gap in the bulk spectrum opened by this avoided crossing does not span the entire Brillouin zone in k_z . The spectral weight of the surface-derived feature therefore lies within the manifold of bulk states which disperse around this avoided crossing. It is therefore better defined as a surface resonance rather than a true surface state. Consistent with this, we find that its wavefunction is more extended below the surface than for TSS2 (Supplemental Fig. S2). Nonetheless, clear signatures of its in-plane Dirac-like dispersion are visible in our ARPES measurements at selected photon energies (Fig. 2(c)), while our spin-resolved measurements (Fig. 2(e)) reveal that it retains the spin-momentum locking characteristic of a TSS. Excitingly, therefore, our findings reveal how the band inversion created by the crossing of p -orbital E and A_1 -like bands in PdTe_2 drives the formation of a topological state (we refer to this as TSS1) whose topological origin still requires its existence despite the additional presence of bulk states at the same energies and in-plane momenta, thereby creating a topological surface resonance.

Intriguingly, we find an additional two-dimensional state evident as a non-dispersive feature in Fig. 2(b) that is pinned at exactly the energy of the bulk Dirac point. Tracking this state slightly away from the Dirac point along the $\bar{\Gamma} - \bar{M}$ in-plane direction, we find that it hosts a strong in-plane spin polarisation with the same sign as the upper branch of TSS1 (labeled SS in Fig. 2(e,f); see also Supplemental Fig. S3 which shows that this develops some out-of-plane spin canting along $\bar{\Gamma} - \bar{K}$). While spin-polarised Fermi arc surface states are known to form between the surface projection of neighbouring bulk Dirac points,^{25,26} they would not naturally be expected here for the (001) cleavage surface of PdTe_2 where the two bulk Dirac points project exactly on top of each other, shrinking the arc length to zero. We note that topological surface states pinned to the Dirac point have, however, recently been reported in calculations for other type-II bulk Dirac systems.⁴³ The origin of these states requires further investigation, but nonetheless the experimental

observation of an additional spin-polarised surface state here stands as a further example of the rich surface electronic structure that this compound possesses, driven by an intricate array of band inversions within the p -orbital manifold of its bulk electronic structure.

We show in Fig. 3 and Supplemental Fig. S4 how such band inversions can be found in multiple other TMDs with different local and global crystalline symmetries, and which exhibit widely varying bulk properties. We first consider the closely-related compound, 1T-PtSe_2 . This is semi-metallic, with a smaller overlap of chalcogen-derived bonding and anti-bonding states than in PdTe_2 .⁴⁵ The transition metal states again contribute relatively little near to the Fermi level, while the p_z -derived chalcogen band can be clearly resolved cutting through the $p_{x,y}$ -derived states in the vicinity of E_F (Fig. 3(a)). A single tilted bulk Dirac cone and a pair of TSSs are stabilised in the occupied electronic structure just as for PdTe_2 . These are evident in our supercell calculations (Fig. 3(b)) and well matched by our experimental ARPES measurements (Fig. 3(c,d)). The spin-orbit coupling of the Se manifold is weaker than that of Te, evident from both the smaller splitting between E -like states and from smaller anti-crossing gaps which open in the vicinity of unprotected band crossings. The local band gaps in which the TSSs reside are therefore smaller than in PdTe_2 , causing the upper branches of the TSSs to rapidly “turn over” to maintain the surface-bulk connectivity as required by their topological origin.

Nonetheless, in contrast to the common picture for well-known topological insulators such as Bi_2Se_3 , the band inversions leading to such topological surface states, as well as the bulk Dirac cone formation, naturally survive this reduction in spin-orbit coupling strength. Indeed, the relevant energy scales for stabilising the topological surface states here are the p_z -derived bandwidth vs. the trigonal crystal field splitting. While increased spin-orbit coupling strength will open larger hybridisation gaps, our findings (see Fig. 3(c,d)) demonstrate how the topological surface states survive as topological surface resonances even in the limit where the hybridisation gap opened is significantly smaller than the dispersion of bulk electronic states around this. They should therefore be a very robust feature of the intrinsic p -orbital band inversions found here.

We note that the recent observation of a type-II BDP in PtTe_2 can be understood within the same classification that we present here,⁴⁶ seemingly establishing our findings as generic to the group-10 TMD metals and semi-metals.⁴⁷ Our findings are not limited to group-10 TMDs, however, and we show in Supplemental Fig. S4(a,b) how a very similar set of bulk band crossings/inversions occurs for the high-temperature 1T phase of the group-9 TMD IrTe_2 . Here, the resulting bulk Dirac point can be expected to occur in close proximity to the Fermi level (where a small amount of doping could be used to tune it

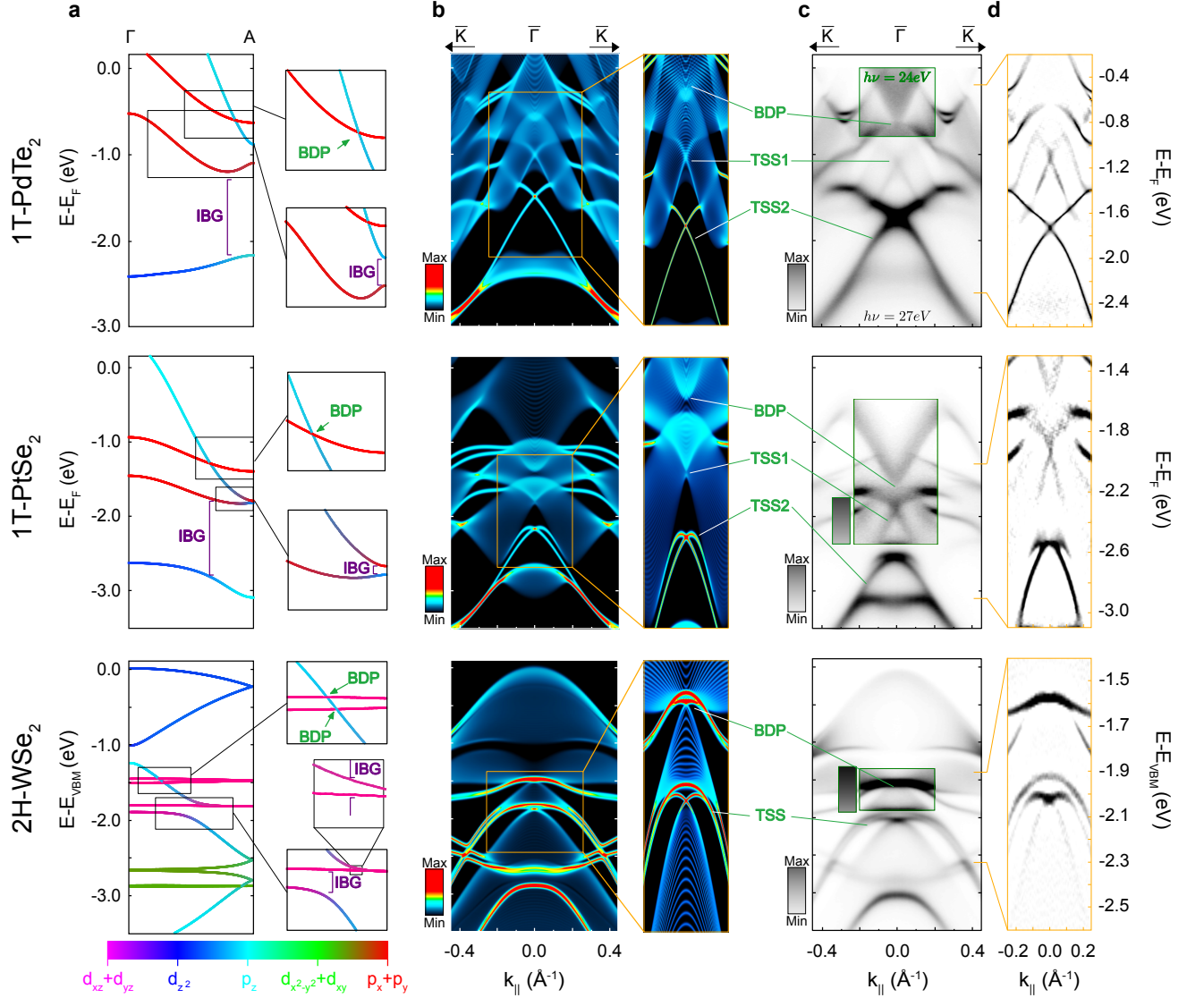


FIG. 3. **Generic observation of bulk Dirac fermions and topological surface states in TMDs.** (a) Orbitaly-resolved out-of-plane bulk electronic structure of (top to bottom) PdTe₂, PtSe₂, and WSe₂, revealing the formation of bulk Dirac points (BDPs) and inverted band gaps (IBGs) as discussed in the text. (b) Surface-projected supercell calculations (along $\bar{\Gamma} - \bar{K}$), (c) ARPES measurements (top to bottom: $\hbar\nu = 27$ eV, p -pol; $\hbar\nu = 64$ eV, p -pol; $\hbar\nu = 49$ eV, CR+CL polarisation) and (d) corresponding curvature analysis⁴⁴ show the surface-projected electronic structure of each compound, revealing the presence of the bulk Dirac cones as well as topological surface states located within the IBGs. The insets in (c) show the ARPES data measured with a different photon energy (PdTe₂, $\hbar\nu = 24$ eV) or shown with a different colour contrast (PtSe₂ and WSe₂) to better highlight some key features of the data.

exactly to E_F), making our findings directly relevant to transport properties of this material. Furthermore, the trigonal symmetry which protects the BDP is lost upon cooling through a structural phase transition,^{48,49} raising prospects to investigate temperature-driven topological phase transitions and mass gap opening of the type-II Dirac fermions.

Our findings are also not limited to the 1T polymorph of TMDs. We show in Fig. 3 how similar states are stabilised in the 2H structure of WSe₂ (space group:

$P6_3/mmc$), albeit with some important differences to the case of PdTe₂. Our bulk band structure calculations along k_z (Fig. 3(a)), which are in good agreement with previous photon energy-dependent ARPES measurements,⁵ reveal a strongly dispersive band with significant p_z orbital character, intersected by very weakly dispersing bands at around 1.5 and 1.9 eV (2.7 and 2.9 eV) below the valence band top which we attribute as the anti-bonding (bonding) E -like bands, respectively, in analogy with the discussions above. We note that, un-

like for PdTe₂, the Fermi level lies in a band gap of both the transition-metal (formally in a d^2 configuration) and chalcogen-derived states, and so this system is a semiconductor. Moreover, transition-metal and chalcogen-derived states are no longer well separated in energy, and so the E -like bands have a strong transition-metal d -orbital character intermixed with their Se $p_{x/y}$ character. The more localised nature of the d vs. p orbitals together with an increased inter-layer separation leads to a significantly smaller out-of-plane dispersion of these E -like bands than for PdTe₂. Finally, the unit cell contains two MX₂ (M=transition metal, X=chalcogen) layers in the 2H structure, as compared to a single such layer in the 1T structure. This results in an effective backfolding of the bands about the Brillouin zone boundary along k_z , doubling each of the $R_{5,6}^\pm$ and $R_{4'}^\pm$ bands as seen in our calculations.

The symmetry-enforced degeneracy of the R_4 - $R_{5,6}$ crossings arising from the three-fold rotational symmetry discussed in our simple model above, however, still holds. Now, therefore, the crossing of the dispersive R_4 band with each of the back-folded $R_{5,6}$ bands leads to a pair of closely-spaced bulk Dirac cones. These are almost maximally tilted, with a strongly-dispersing band crossing almost dispersion-less bands along k_z and, unlike for PdTe₂, they now additionally host significant transition-metal character at the BDP. We observe clear spectral signatures of the in-plane dispersion of these Dirac cones (Fig. 3(c)), but are unable to resolve a splitting of the two cones due to their small energy separation and strong three-dimensional dispersions. Both crossings of the R_4 and back-folded $R_{4'}$ bands become gapped, and would therefore be expected to host topological surface states/resonances as in PdTe₂. One such band gap is too small to resolve experimentally, while for the lower branch a clear inverted band gap is opened. Our supercell calculations (Fig. 3(b)) indeed reveal the TSS located within this band gap, spanning between the manifold of bulk states above and below the band gap. Although the resulting band gap is small, the in-plane dispersion is significant, and our ARPES and spin-ARPES measurements (Fig. 3(c) and Supplemental Fig. S5) show clear evidence for the existence of the resulting surface state, its band-gap crossing nature, and its chiral spin polarisation. As shown in Supplemental Fig. S4(c-f), we find similar bulk Dirac cones and inverted band gaps in other 2H-structured TMDs, TaSe₂ and NbSe₂ (space group: P6₃/mmc), despite them hosting a different layer stacking sequence as compared to WSe₂. This opens the exciting prospect to investigate the influence of charge order, which these compounds host, and the consequent reconstruction of the electronic structure, on the topological and bulk Dirac states.

While the principle underlying the formation of bulk Dirac cones and topological surface states here is very general, our demonstration of their existence across mul-

tiples TMDs indicates that there is still significant opportunity to tailor the properties and locations of these states. Moreover, similar arrays of band inversions can naturally be expected arising within a single orbital manifold in a variety of other compounds. Even within the TMD family, by controlling the crystal symmetry, the magnitude of the crystal field splitting, and the filling of the d -derived states, it is possible to isolate the chalcogen-derived band inversions, to move them to the Fermi level, or to drive their direct interplay with transition-metal d -electrons. Exploiting this will open new prospects for the rational design of topological materials, and indicates just how wide their purview can be expected to be.

Methods

Calculations: The bulk calculations were performed within density functional theory (DFT) using Perdew-Burke-Ernzerhof exchange-correlation functional as implemented in the WIEN2K program.⁵⁰ Relativistic effects including spin-orbit coupling were fully taken into account. For all atoms, the muffin-tin radius R_{MT} was chosen such that its product with the maximum modulus of reciprocal vectors K_{max} become $R_{MT}K_{max} = 7.0$. The Brillouin zone sampling of 1T (2H) structures was carried out using a $20 \times 20 \times 20$ ($20 \times 20 \times 10$) k -mesh. For the surface calculations, a 100 unit tight binding supercell was constructed using maximally localized Wannier functions.⁵¹⁻⁵³ The p -orbitals of the chalcogen and the d -orbitals of the transition metal atoms were chosen as the projection centres.

ARPES: ARPES measurements of PdTe₂ and PtSe₂ were performed at the I05 beamline of Diamond Light Source, UK, and most spin-integrated WSe₂ measurements at the CAS-SIOPEE beamline of Synchrotron SOLEIL, France. Additional ARPES measurements of WSe₂ were taken at the APE beamline of Elettra Sincrotrone Trieste, Italy, along with the majority of the spin-resolved ARPES measurements. Additional spin-resolved measurements of PdTe₂ were obtained from the I3 beamline of MAX IV Laboratory, Sweden.

High-quality single crystal samples, grown by chemical vapour transport, were cleaved *in situ* at temperatures ranging between 9-15K. Measurements were performed using either p-polarised (PdTe₂, PtSe₂, WSe₂), or circularly polarised (WSe₂) light, and using photon energies in the range $h\nu = 24 - 132$ eV. Scienta R4000 hemispherical analysers, with a vertical entrance slit and the light incident in the horizontal plane, were used at Diamond and SOLEIL.

A VG-Scienta DA30 analyser (Elettra), fitted with two very low energy electron diffraction (VLEED) based spin polarimeters, was utilised for the majority of the spin-resolved measurements along three momentum directions, while additional measurements were performed using a mini-Mott setup on a Scienta R4000 analyser (Max IV). The finite spin-detection efficiency was corrected using detector-dependent Sherman functions ranging between $S = 0.17 \pm 0.03$ and $S = 0.43 \pm 0.03$ as determined by fitting the spin-polarisation of reference measurements of the Au(111) Rashba-split surface state for each experimental set-up utilised. Spin-resolved EDCs were determined according to

$$I_i^{\uparrow,\downarrow} = \frac{I_i^{\text{tot}}(1 \pm P_i)}{2}, \quad (1)$$

where $i = \{x, y, z\}$, $I_i^{\text{tot}} = (I_i^+ + I_i^-)$ and I_i^{\pm} is the measured intensity for a positively or negatively magnetised detector, corrected by a relative efficiency calibration. The final spin polarisation is defined as follows:

$$P_i = \frac{I_i^+ - I_i^-}{S(I_i^+ + I_i^-)}, \quad (2)$$

where S is the relevant Sherman function for the detector in use.

Quantitative spin-polarisation magnitudes were determined from the relative areas of Lorentzian peak fits to energy distribution curves (EDCs) originating from oppositely magnetised detectors. A Shirley background and Gaussian broadening were included in this analysis.

To determine the PdTe_2 k_z dispersion from photon-energy-dependent ARPES, we employed a free electron final state model

$$k_z = \sqrt{\frac{2m_e}{\hbar^2}}(V_0 + E_k \cos^2 \theta)^{1/2} \quad (3)$$

where θ is the in-plane emission angle and V_0 is the inner potential. We find best agreement to density-functional theory calculations taking an inner potential of 16 eV and a c -axis lattice constant of 5.13 Å.

Acknowledgements We thank R. Arita and N. Nagaosa for useful discussions and feedback. We gratefully acknowledge support from the Leverhulme Trust, the Engineering and Physical Sciences Research Council, UK (Grant Nos. EP/M023427/1 and EP/I031014/1), the Royal Society, the Japan Society for Promotion of Science (Grant-in-Aid for Scientific Research (S); No. 24224009), the International Max-Planck Partnership for Measurement and Observation at the Quantum Limit and the Research Council of Norway (Project No. 250985/F20) for Fundamentals of low-dissipation topological matter in the Frinatek program. B.-J. Y was supported by IBS-R009-D1, Research Resettlement Fund for the new faculty of Seoul National University, and Basic Science Research Program through the National Research Foundation of Korea (NRF) funded by the Ministry of Education (Grant No. 0426-20150011). OJC, LB, JMR and VS acknowledge EPSRC for PhD studentship support through grant Nos. EP/K503162/1, EP/G03673X/1, EP/L505079/1, and EP/L015110/1. IM acknowledges PhD studentship support from the IMPRS for the Chemistry and Physics of Quantum Materials. We thank Diamond Light Source (via Proposal Nos. SI9500, SI12469, SI13438, and SI14927) Elettra, SOLEIL, and Max-Lab synchrotrons for access to Beamlines I05, APE, CASSIOPEE, and i3, respectively, that contributed to the results presented here.

-
- [1] Lui, H. *et al.* Polytypism, polymorphism, and superconductivity in $\text{TaSe}_{2-x}\text{Te}_x$. *PNAS* **112**, E1174–E1180 (2015).
 [2] Morosan, E. *et al.* Superconductivity in Cu_xTiSe_2 . *Nature Phys.* **2**, 544–550 (2006).

- [3] Li, L. J. *et al.* Controlling many-body states by the electric-field effect in a two-dimensional material. *Nature* **529**, 185–189 (2015).
 [4] Xu, X., Yao, W., Xiao, D. & Heinz, T. F. Spin and pseudospins in layered transition metal dichalcogenides. *Nature Phys.* **10**, 343–350 (2014).
 [5] Riley, J. M. *et al.* Direct observation of spin-polarized bulk bands in an inversion-symmetric semiconductor. *Nature Phys.* **10**, 835–839 (2014).
 [6] Wilson, J. A., Di Salvo, F. J. & Mahajan, S. Charge-Density Waves in Metallic, Layered, Transition-Metal Dichalcogenides. *Phys. Rev. Lett.* **32**, 882–885 (1974).
 [7] Borisenko, S. V. *et al.* Pseudogap and Charge Density Waves in Two Dimensions. *Phys. Rev. Lett.* **100**, 196402 (2008).
 [8] Rohwer, T. *et al.* Collapse of long-range charge order tracked by time-resolved photoemission at high momenta. *Nature* **471**, 490–493 (2011).
 [9] Wang, Q. H., Kalantar-Zadeh, K., Kis, A., Coleman J. N. & Strano, M. S. Electronics and optoelectronics of two-dimensional transition metal dichalcogenides. *Nature Nano.* **7**, 669–712 (2012).
 [10] Yokoya, T. *et al.* Fermi Surface Sheet-Dependent Superconductivity in 2H-NbSe_2 . *Science* **294**, 2518–2520 (2001).
 [11] Mak, K. F., Lee, C., Hone, J., Shan, J. & Heinz, T. F. Atomically Thin MoS_2 : A New Direct-Gap Semiconductor. *Phys. Rev. Lett.* **105**, 136805 (2010).
 [12] Xiao, D., Liu, G.-B., Feng, W., Xu, X. & Yao, W. Coupled Spin and Valley Physics in Monolayers of MoS_2 and Other Group-VI Dichalcogenides. *Phys. Rev. Lett.* **108**, 196802 (2012).
 [13] Ritschel, T. *et al.* Orbital textures and charge density waves in transition metal dichalcogenides. *Nature Phys.* **11**, 328–331 (2015).
 [14] Riley, J. M. *et al.* Negative electronic compressibility and tunable spin splitting in WSe_2 . *Nature Nano.* **10**, 1043–1047 (2015).
 [15] Ugeda, M. M. *et al.* Characterization of collective ground states in single-layer NbSe_2 . *Nature Phys.* **12**, 92–97 (2016).
 [16] Bawden, L. *et al.* Spin-valley locking in the normal state of a transition-metal dichalcogenide superconductor. *Nature. Commun.* **7**, 11711 (2016).
 [17] Hasan, M. Z., Kane, C. L. Colloquium: Topological insulators. *Rev. Mod. Phys.* **82**, 3045–3067 (2010).
 [18] Young, S. M. *et al.* Dirac Semimetal in Three Dimensions. *Phys. Rev. Lett.* **108**, 140405 (2012).
 [19] Liu, Z. K. *et al.* Discovery of a Three-Dimensional Topological Dirac Semimetal, Na_3Bi . *Science* **343**, 864–867 (2014).
 [20] Wang, Z. *et al.* Dirac semimetal and topological phase transitions in A_3Bi ($\text{A}=\text{Na}, \text{K}, \text{Rb}$). *Phys. Rev. B.* **85**, 195320 (2012).
 [21] Wang, Z. *et al.* Three-dimensional Dirac semimetal and quantum transport in Cd_3As_2 . *Phys. Rev. B* **88**, 125427 (2013).
 [22] Borisenko, S. *et al.* Experimental Realization of a Three-Dimensional Dirac Semimetal. *Phys. Rev. Lett* **113**, 027603 (2014).
 [23] Yang, B.-J., Nagaosa, N. *et al.* Classification of stable three-dimensional Dirac semimetals with nontrivial topology. *Nature Commun.* **5**, 4898 (2014).
 [24] Yang, B.-J., Morimoto, T., Furusaki, A. Topological

- charges of three-dimensional Dirac semimetals with rotation symmetry. *Phys. Rev. B* **92**, 165120 (2015).
- [25] Xu, S.-Y. *et al.* Observation of Fermi arc surface states in a topological metal. *Science* **347**, 294-298 (2015).
- [26] Yi. H. *et al.* Evidence of Topological Surface State in Three-Dimensional Dirac Semimetal Cd_3As_2 . *Sci. Rep.* **4**, 6106 (2014).
- [27] Xu, S.-Y. *et al.* Discovery of a Weyl fermion semimetal and topological Fermi arcs. *Science* **349**, 613-617 (2015).
- [28] Yang, L. X. *et al.* Weyl semimetal phase in the non-centrosymmetric compound TaAs. *Nature Phys.* **11**, 728-732 (2015).
- [29] Lv., B. Q. *et al.* Observation of Weyl nodes in TaAs. *Nature Phys.* **11**, 724-727 (2015).
- [30] Wan, X. *et al.* Topological semimetal and Fermi-arc surface states in the electronic structure of pyrochlore iridates. *Phys. Rev. B* **83**, 205101 (2011).
- [31] Weng, H. *et al.* Weyl Semimetal Phase in Noncentrosymmetric Transition-Metal Monophosphides. *Phys. Rev. X* **5**, 011029 (2015).
- [32] Lv. B. Q. *et al.* Experimental Discovery of Weyl Semimetal TaAs. *Phys. Rev. X* **5**, 031013 (2015).
- [33] Borisenko, S. *et al.* Time-Reversal Symmetry Breaking Type-II Weyl State in YbMnBi_2 . *arXiv:1507.04847* (2016).
- [34] Soluyanov A. A., *et al.* Type-II Weyl semimetals. *Nature* **527**, 495-498 (2015).
- [35] Zhang, H. *et al.* Topological insulators in Bi_2Se_3 , Bi_2Te_3 and Sb_2Te_3 with a single Dirac cone on the surface. *Nature Phys.* **5**, 438-442 (2009).
- [36] Wu, Y. *et al.* Observation of Fermi arcs in the type-II Weyl semimetal candidate WTe_2 . *Phys. Rev. B* **94**, 121113(R) (2016).
- [37] Belopolski, I. *et al.* Criteria for Directly Detecting Topological Fermi Arcs in Weyl Semimetals. *Phys. Rev. Lett.* **116**, 066802 (2016).
- [38] Furuseth, S. *et al.* Redetermined Crystal Structures of NiTe_2 , PdTe_2 , PtS_2 , PtSe_2 , and PtTe_2 . *Acta Chemica Scandinavica* **19**, 257-258 (1965).
- [39] Raub C. J. *et al.* The occurrence of superconductivity in sulfides, selenides, tellurides of Pt-group metals. *Journal of Physics and Chemistry of Solids* **26**, 2051-2057 (1965).
- [40] Fei, F. *et al.* Nontrivial Berry phase and type II Dirac transport in layered material PdTe_2 . *arXiv:1611.08112* (2016).
- [41] We note that a very recent arXiv posting (1612.06946) also reports the observation of type-II Dirac fermions in PdTe_2 , consistent with our findings.
- [42] Yan, L. *et al.* Identification of Topological Surface State in PdTe_2 Superconductor by Angle-Resolved Photoemission Spectroscopy. *Chinese Phys. Lett.* **32**, 067303 (2015).
- [43] Chang, T.-R. *et al.* Type-II Topological Dirac Semimetals: Theory and Materials Prediction (VAL_3 family). *arXiv:1606.07555*, (2016).
- [44] Zhang, P. *et al.* A precise method for visualizing dispersive features in image plots. *Rev. of Sci. Instruments* **82**, 4 (2011).
- [45] Guo. G. Y. & Liang, W. Y. The electronic structures of platinum dichalcogenides: PtS_2 , PtSe_2 and PtTe_2 . *J. Phys. C: Solid State Phys.* **19**, 995 (1986).
- [46] Yan, M. *et al.* Lorentz-violating type-II Dirac fermions in transition metal dichalcogenide PtTe_2 . *arXiv:1607.03643* (2016).
- [47] Huang, H., Zhou, S., Duan, W. Type-II Dirac fermions in the PtSe_2 class of transition metal dichalcogenides. *Phys. Rev. B* **94**, 121117(R) (2016).
- [48] Cao, H. *et al.* Origin of the phase transition in IrTe_2 : Structural modulation and local bonding instability. *Phys. Rev. B* **88**, 115122 (2013).
- [49] Fang, A. F. *et al.* Structural phase transition in IrTe_2 : A combined study of optical spectroscopy and band structure calculations. *Sci. Rep.* **3**, 1153 (2013).
- [50] Balaha, P. *et al.* WIEN2K package, Version 13.1 (2013).
- [51] Souza, I. *et al.* Maximally localized Wannier functions for entangled energy bands. *Phys. Rev. B* **65**, 035109 (2001).
- [52] Mostofi, A. A. *et al.* Wannier90: a tool for obtaining maximally localized Wannier functions. *Comp. Phys. Commun.* **178**, 685-699 (2008).
- [53] Kunes, J. *et al.* WIEN2WANNIER: from linearized augmented plane waves to maximally localized Wannier functions. *Comp. Phys. Commun.* **181**, 1888-1895 (2010).